J Mater Sci: Mater Electron (2026) 37:1230

Synthesis, characterization and analysis of new nanoflakes and nanoparticles using amphoteric and cationic additives for humidity sensing applications

Soo Ping Kok[1], Yun Ii Go[1,*], Siti Barirah Ahmad Anas[2], M. L. Dennis Wong[3,4], and Kah Yoong Chan[5]

[1] *School of Engineering and Physical Sciences, Heriot-Watt University Malaysia, 62200 Putrajaya, Malaysia*
[2] *Wireless and Photonics Networks Research Centre, Faculty of Engineering, Universiti Putra Malaysia, 43400 Serdang, Malaysia*
[3] *School of Engineering, Newcastle University, Newcastle Upon Tyne NE1 7RU, UK*
[4] *Newcastle University Medicine Malaysia, 79200 Educity, Johor, Malaysia*
[5] *Faculty of Artificial Intelligence and Engineering, Multimedia University, Cyberjaya, Malaysia*

Received: 14 March 2026
Accepted: 16 May 2026

ABSTRACT

Regulations have been established across various industries, especially in food and agriculture industries, due to the importance in maintaining optimal humidity level. Excessive humidity led to risk of microbial growth, whereas dry conditions caused adverse effects in product quality. Among all the studies, modification in surface morphology for the increase in surface area and active sites has been reported as a critical approach for the enhancement of humidity sensing. Both amphoteric and cationic surfactants are organic compounds which act as an effective structure regulator for the synthesis of reactive materials, owing to their capability in forming high porosity nanostructure for increase water-surface interaction. In this study, hexamethylenetetramine (HMT) and cetyltrimethylammonium bromide (CTAB) were selected for the modification of surface morphology of tin dioxide (SnO_2) and zinc oxide (ZnO). Precursor solutions of additive-enhanced SnO_2 and ZnO were coated onto glass substrates for morphology characterization. Hygroscopicity test was carried out to examine the interaction between the synthesized nanostructures and the ambient moisture. The effect of additive concentration towards change in material properties was investigated. The observation from the experiment revealed that equimolar additive and reactive material at 0.010 M enhanced the water-surface interaction of metal oxide nanostructures significantly. This allows the nanostructures to be used as a reactive material for humidity sensors, enabling applications in humidity-sensitive industries.

Address correspondence to E-mail: y.go@hw.ac.uk

https://doi.org/10.1007/s10854-026-17561-w
Published online: 01 June 2026

1 Introduction

1.1 Humdity sensing mechanism

Relative humidity (RH) refers to the water vapor saturation of air in comparison with the maximum amount that can be held at a specific temperature. Humidity sensing refers to the measurement of moisture, usually express as RH [1]. The sensing mechanism is based on adsorption and desorption of water molecules by the hygroscopic nanostructure, which changes the optical or electrical properties of the sensor [2]. At lower RH level, the adsorption mechanism is dominant by chemisorption, where chemical bonds such as covalent, metallic, or ionic form between functional groups and surface of nanostructure [3]. With RH level increasing, the physisorption become dominant, where water molecules accumulate on the active sites of nanostructure via weak Van der Waals forces, forming mono- or multilayer adsorption. The continuous increase of RH led to capillary condensation, where vapor condenses within the pores of nanostructures. At this stage, the water molecules trapped within the pores of nanostructure and leading to poor desorption. Hysteresis may occur due to the capillary condensation at high RH. It is an irreversible process for the nanostructure to return to its original form, jeopardizing the water adsorption and desorption process and impacting the sensors response time and accuracy [4]. Humidity sensors require high sensitivity and accuracy, good linearity, fast response or recovery times, and high repeatability to meet industry standards for multiple applications [5]. For food and beverages, processing, storage, and distribution require high accuracy humidity sensors to maintain product quality [6]. Dry storage at RH from 50 to 70% are effective in reducing average bacterial populations [7]. For long period cold storage, a near saturated RH for more than 90% reduces water loss, maintains the color and texture, and prolongs the lipid peroxidation of fresh foods [8, 9].

1.2 Reactive material for humidity-sensitive industries

For agriculture applications, including greenhouse air monitoring, soil moisture detection, and dew prevention, humidity sensors are necessary to increase crops yield [10]. The RH requirements of green house for optimal crops growth usually range between 50 to 80%RH [11]. The plant leaves show best performance of color and chemical composition at 70%RH [12]. The germination process is improved under 80%RH for plant sprouting [13]. Maintaining RH below 80% is also important to prevent disease among crops [14].

Carbon-based materials have been investigated for humidity sensing in smart packaging of food and pharmaceutical products [15]. Various modification techniques including doping, nanocomposites, and surface modification have demonstrated improvement in humidity sensing performance. In addition, ceramics and polymer-based materials have been studied for tracking food decomposition [16]. The result reported that enhanced sensitivity and selectivity of electronic responses to the targeted analytes can be achieved. Coating polymer-based materials on optical fibre sensors has also been developed for improved functionality, measurement range, sensitivity, and linearity in agriculture humidity sensing [17]. Other than that, metal oxide-based material such as lanthanum ferrite ($LaFeO_3$), zinc oxide (ZnO), and titanium dioxide (TiO_2) has been explored for moisture detection for agriculture applications [18–20].

The materials exhibited improved sensitivity, high stability after long period deployment, and good sensor response for moisture detection of different soil samples. The tunable surface morphology to increase surface area is another advantage of metal oxide-based materials [21]. Both ZnO and tin dioxide (SnO_2) can be synthesized into nanoflower, nanoparticle, nanorod, and other surface morphology as illustrated in Fig. 1 via various synthesis techniques [22–24]. These surface morphology with high porosity and large surface area improved the water-surface interaction by increase the active sites for water adsorption and desorption mechanism, leading towards improved humidity sensing performance [25]. On the contrary, surface morphology with clustering limits the surface area and therefore result in lower sensitivity in humidity sensing applications [26].

To meet the market challenges, humidity sensors based on nanomaterials have been under development for enhanced reliability and accuracy [27]. However, the sensor response, sensitivity, hysteresis, and reliability of hygroscopic nanomaterials require further improvement in broadening sensing applications. Various techniques such as doping, nanocomposite, or surface modification have been explored to enable advanced sensing technology [28, 29]. Additive-enhanced technique has been reported as one of the

surface modification techniques that enhance sensing performance of pure metal oxide materials [30].

The amphoteric and cationic surfactants are common additives that influence the nucleation for the formation of various morphology in nanostructures [31]. The amphoteric surfactant exhibits larger headgroups compared to surfactants from other categories, leading to formation of micelle around the cluster of nanoparticles [32]. This material properties result in uniformly distributed porous structure, which increase the water-surface interaction [33]. The cationic surfactant possesses capability in self-assembly, corrosion resistance, and provides stability in micelles formation during synthesis of nanostructure [34]. The long chain of carbon atoms of cationic surfactant also helps to prevent agglomeration, increasing the porosity of formed nanostructures [35]. The applications of the additives and their effect on metal oxide were illustrated in Table 1, while different nanostructure and their humidity sensing mechanisms were listed in Table 2.

The hexamethylenetetramine (HMT) and cetyltrimethylammonium bromide (CTAB) are amphoteric and cationic surfactants which demonstrate high

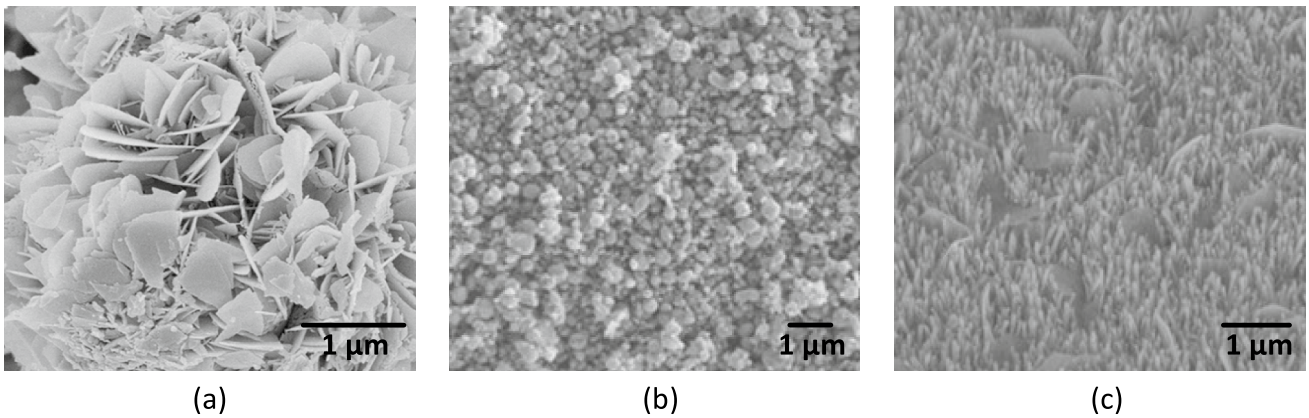

Fig. 1 Morphology of **a** SnO_2 nanoflower synthesize via hydrothermal technique. Adapted from [22], **b** ZnO nanoparticle synthesize via controlled chemical reaction. Adapted from [23], and **c** ZnO nanorods synthesize via hydrothermal technique. Adapted with permission from [24]

Table 1 Application of amphoteric and cationic additives in metal oxide

Reactive material	Additive	Role of additive	Application	Refs
Titanium dioxide-nickel (II) oxide (TiO_2–NiO)	Laurylamine hydrochloride (LAHC)	Formation of mesoporous nanostructure	Not reported	[38]
TiO_2	CTAB	Increase porosity	Gas sensing	[39]
ZnO	CTAB	Redistribution of crystallite grains	Not reported	[37]
ZnO	HMT	Promoting anisotropic growth	Gas sensing	[36]
ZnO	CTAB	Formation of nanoflake	Humidity sensing	This work
SnO_2	HMT	Formation of nanoparticle	Humidity sensing	This work

Table 2 Humidity sensing mechanism of various nanostructure

Nanostructure	Mechanism	Achievement	Ref
SnO_2 nanostructure	Surface adsorption via hydrogen bond	Increase conductivity of electrical sensor	[40]
ZnO/SnO_2 nanocomposite	Increase oxygen vacancies	Fast response and recovery speed	[41]
SnO2/MCM-48 mesoporous	Surface adsorption via hydrogen bond	High surface area	[42]
Additive-enhanced ZnO and SnO_2	Additive-controlled porous network	Enable optical fibre humidity sensing	This work

compatibility with metal oxide, acting as structure-directing agents in modifying surface morphology of pure metal oxide. HMT-enhanced ZnO has been investigated for sensing applications, the role of HMT in promoting anisotropic growth leading to improved sensing properties of the ZnO nanostructures has been reported [36]. Whereas CTAB has demonstrated the capability in redistribution of crystallite grains of ZnO to achieve improved structural and optical properties [37]. To the best of our knowledge, applications of HMT and CTAB as amphoteric and cationic surfactants to achieve additive-controlled morphology and their impact towards humidity sensing properties of SnO_2 and ZnO have yet to be examined. This paper aims to investigate the optimal stoichiometric balance between precursor and additive by examining the effect of HMT and CTAB concentration via hygroscopicity test and material characterization. The paper also aims to examine the correlation between material characteristics such as water adsorption–desorption behavior, porosity, aggregation with humidity sensing performance by conduct optical spectrum analysis upon coating the additive-enhanced metal oxide onto one of the optical fibre sensors for real-life applications.

2 Materials and methods

2.1 Hydrothermal synthesis

The hydrothermal synthesis allows chemical reactions within aqueous solution under high pressure and temperature, creating high purity materials with tunable morphology [43]. The synthesis method as shown in Fig. 2, which has been reported in previous paper [44], involved preparation of precursor solution by mixture of tin (II) chloride dihydrate ($SnCl_2{\cdot}2H_2O$) or zinc acetate dihydrate ($Zn(CH_3COO)_2{\cdot}2H_2O$) with ethanol and NaOH and proceed with sonication. The drop cast samples were subject to oven which preset to 140 °C for 3 h annealing. The HMT acted as the additive during the synthesis of SnO_2 whereas the CTAB was selected as the additives for synthesis of ZnO. The concentration of SnO_2 and ZnO were fixed at 0.010 M, which is 2256.4 and 2195.0 mg respectively. While the additive concentration increased and decreased as illustrated in Fig. 3, where 2803.80, 1401.90 mg, and 700.95 of HMT and 7289.00, 3644.50, and 1822.25 mg of CTAB were added to achieve concentration of 0.020, 0.010, and 0.005 M, respectively.

2.2 Hygroscopicity test

Various techniques have been applied to quantify the moisture content or water uptake in nanomaterials, including gravimetric, dynamic vapor sorption (DVS), and quartz crystal microbalance (QCM). A gravimetric test method provides adsorption–desorption analysis when target material interacts with water vapor by high precision weighing. The water uptake or loss is recorded under defined duration to characterize the hygroscopicity, given by [45]:

$$Mass\ Uptake = \frac{m_t - m_0}{m_0} \quad (1)$$

where m_t refer to the mass of the reactive material after water adsorption, and m_0 refer to mass of the oven-dry reactive material.

DVS is an automated gravimetric method, where the RH is controlled by flow of carrier gas [46]. This method requires high complex setup of equipment to measure sorption isotherm and is often used to study the state of equilibrium of target material. QCM offer real-time monitoring of adsorption kinetics and allow multiparameter detection up to nanogram scale detection [47]. This test method requires custom signal-processing algorithms and is often applied in chemical or biosensing applications [48]. A modified gravimetric technique was applied for hygroscopicity test in this paper, in accordance to ASTM requirements [49] owing to the low complex equipment setup for testing single material at a time, offering a cost-effective and reliable approach for hygroscopicity assessment in the scale of milligram.

2.3 Material characterization

Various characterization techniques have been conducted in the experiment to understand the molecular composition, material structure, surface morphology, and thermal performance of both SnO_2-HMT and ZnO-CTAB. Fourier Transform Infrared Spectroscopy (FTIR) is a method to identify the fingerprint of the material compound by analyzing the distribution of chemical functional groups based on the interaction between material and IR beam [50]. These chemical functional groups are also important to reveal the

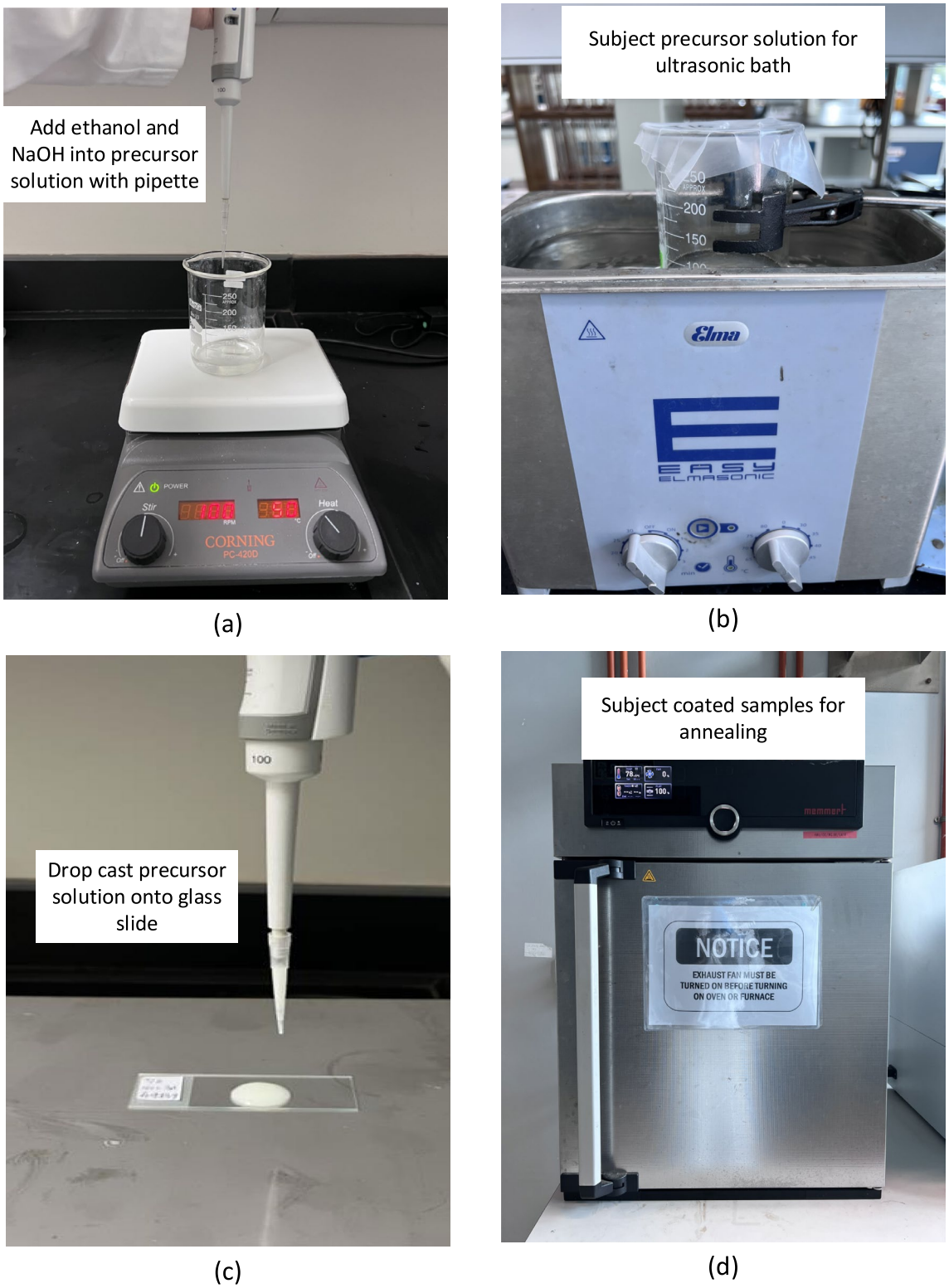

Fig. 2 Lab setup for hydrothermal synthesis involving **a** preparation of precursor solution, **b** sonication, **c** drop cast for sample coating, and **d** annealing

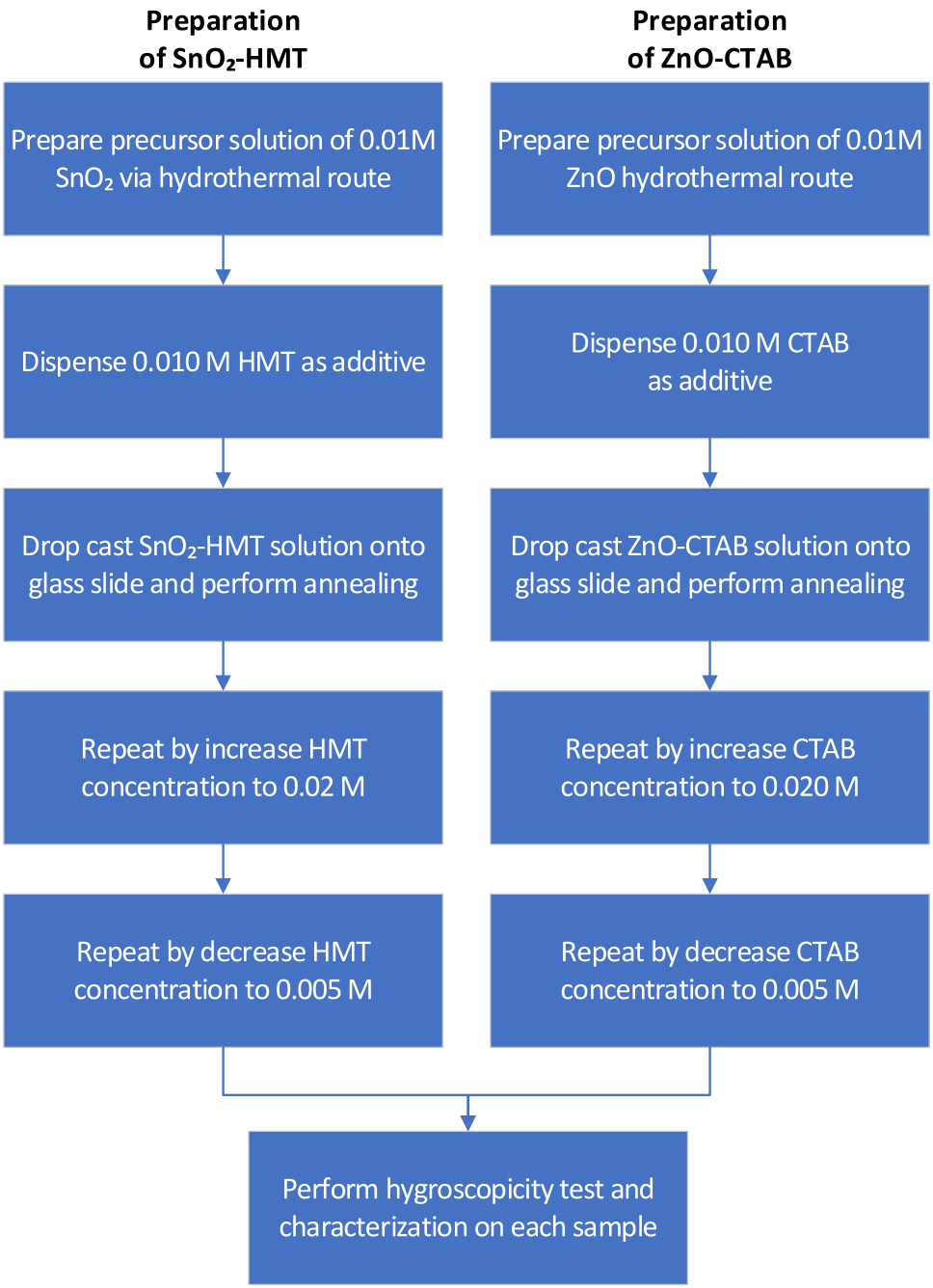

Fig. 3 Block diagram of sample preparation

impact of additive concentration towards reactive material. While the O–H stretching vibration reveals the water-surface interaction of additive-enhanced SnO_2 and ZnO with ambient humidity. The equipment and sample preparation of FTIR involved running initial scan on empty sample holder and placing the solid samples onto sample holder, which cleaned with isopropyl after every use. The IR beam interacted with molecular bonds of the samples and the interferogram signal was captured by the detector. A Fourier transform algorithm was applied to convert the interferogram into an intensity vs. wavenumber curve, known as the FTIR spectra. The illustration of lab setup for sample placement and FTIR spectra acquisition were illustrated in Fig. 4.

Microscope imaging is a low complex visual inspection technique to observe structural changes and provide comparison of reactive material under different

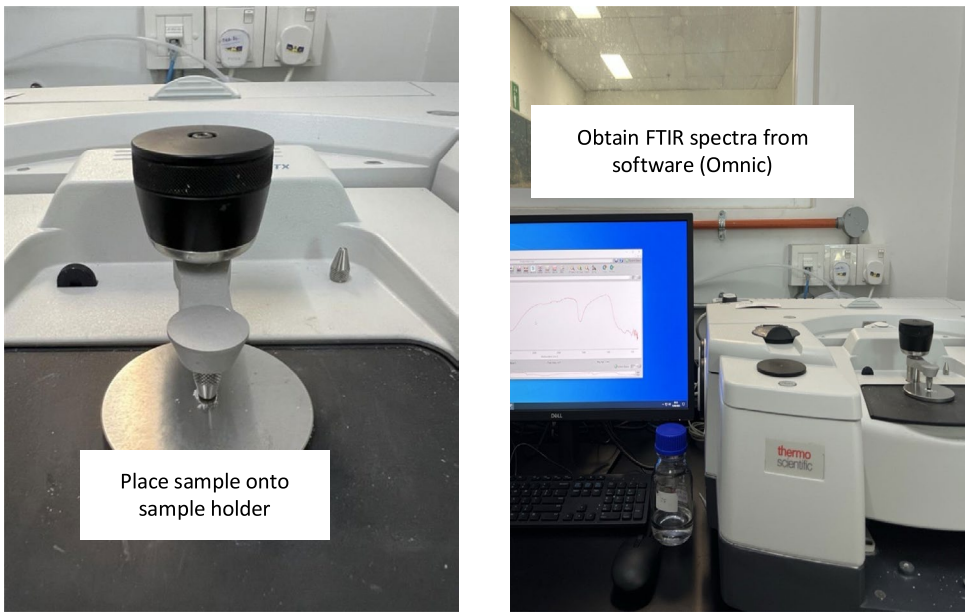

Fig. 4 Lab setup for FTIR involving **a** sample placement and **b** FTIR spectra acquisition

additive concentration. The methods in obtaining microscope images involved placing and securing the glass slide on stage, projecting and adjusting the light source, focusing the lens to obtain images, and continuing fine tuning the lens and light source until a sharp image was observed. The Field Emission Scanning Electron Microscope (FESEM) is important in visualizing the change of material surface morphology under various additive concentration through high resolution imaging in nanoscale. The methodology involved preparing samples by applied gold coating on post-annealed SnO_2-HMT and ZnO-CTAB for conductivity, placing the samples into FESEM chamber under high vacuum, scanning on coated samples with a focused electron beam from a field emission gun, and detecting backscattered electrons to generate high-resolution FESEM images. The illustration of

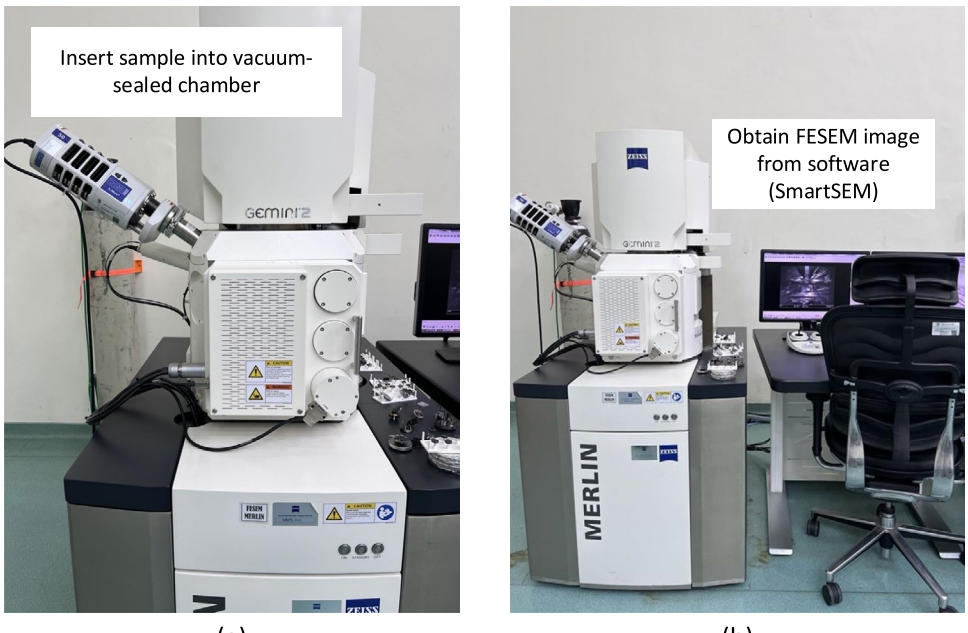

Fig. 5 Lab setup for FESEM involving **a** sample placement and **b** FESEM images acquisition

lab setup for sample placement and FESEM images acquisition were illustrated in Fig. 5.

Thermogravimetric analysis (TGA) was used to measure the thermal decomposition of samples under incremental temperature. This characterization method provides insight towards thermal stability of the reactive materials under various additive concentration. The characterization steps involve placing the sample into furnace under controlled nitrogen atmosphere with flow rate of 30 ml/min, allowing the temperature to heat up from 30 to 500 °C with heating rate of 10 °C/min, and recording the weight vs. temperature curve for comparative study of the weight loss of the metal oxides under different additive concentrations. The illustration of lab setup for sample placement and equipment readiness were illustrated in Fig. 6.

2.4 Optical spectrum analysis

To validate the humidity sensing application of the reactive material, the SnO_2 with 0.01 M HMT was selected for coating onto a FBG with tilted grating profile, which is a type of optical fibre sensor with advantages in high resolution and capability of multiparameter sensing [51]. The sensor is designed to detect shift in transmitted wavelength of the FBG core mode upon expose to environmental change such as temperature, strain, or humidity. The equipment setup, as illustrated in Fig. 7, connected one end of the coated FBG

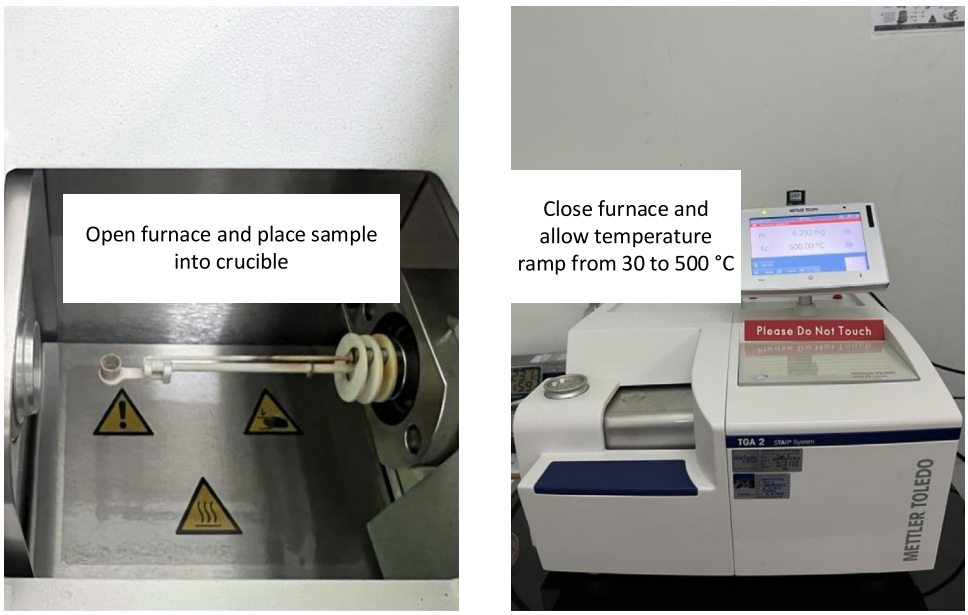

Fig. 6 Lab setup for TGA involving **a** sample placement and **b** equipment readiness

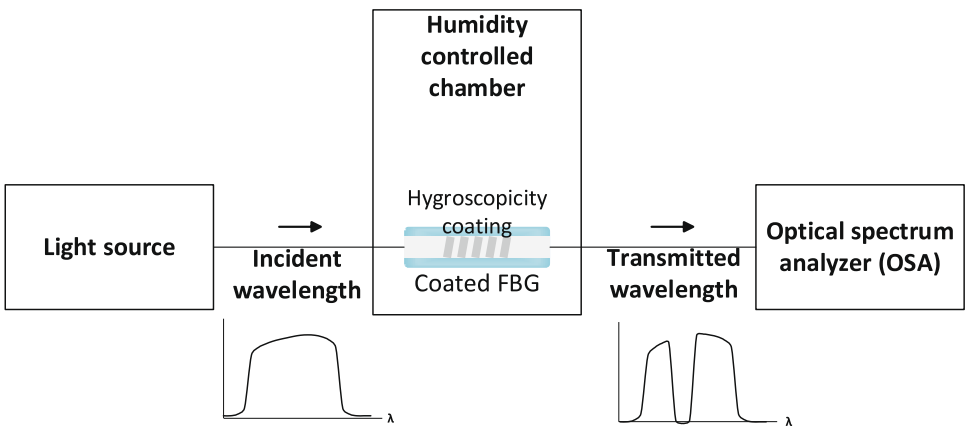

Fig. 7 Illustration of lab setup for optical spectrum analysis

to light source for incident wavelength, and another end to the optical spectrum analyzer (OSA) to record the transmitted wavelength.

3 Result and discussion

3.1 Hygroscopicity test

The hygroscopicity test is a modified gravimetric analysis method to measure water adsorption and desorption by recording the mass change of the reactive material at different humidity level [52]. All six samples obtained from hydrothermal synthesis were inserted into a seal chamber as shown in Fig. 8, where the RH was adjusted by insertion or removal of humidity control substances. The weight change of every 10%RH was recorded from 40 to 80% increase RH, and 80 to 40% decrease RH as illustrated in Figs. 9 and 10. The *m value* and R^2 *value* were calculated based on the mass uptake ratio at different RH levels. Higher *m value* can be interpreted as enhance water adsorption and desorption, higher R^2 *value* can be interpreted as strong correlation of the linear regression model and represent better accuracy of the humidity sensing model. The *m value* and R^2 *value* of respective samples were summarized in Table 3 while the individual mass change of each sample was listed in Table 4. The result showed 0.010 M HMT contributed to the optimized *m value* and R^2 *value* compared to 0.020 and 0.005 M concentration, indicating the best performance in humidity sensing of SnO_2-HMT at equimolar concentrations between the metal oxide and additive. Increasing the HMT concentration led to slightly higher *m value* during decremental RH but leading to lower R^2 *value* as compared to 0.010 M, whereas decreasing the HMT concentration led to lower *m value* and R^2 *value*.

The ZnO-CTAB sample showed highest m value at 0.005 M CTAB concentration, however, the R^2 *value* was low (< 0.9). Minimal water uptake was observed during increasing RH from 50 to 70%RH and during decreasing RH from 60 to 40%RH. With the CTAB concentration decreased to 0.010 M, the *m value* decreased slightly but showed significant improvement in the R^2 *value* (> 0.9). By increasing the CTAB concentration to 0.020 M, the *m value* is approximately 2 × lower compared to 0.010 M. Hence, the equimolar additive concentration was recommended to achieve optimal humidity sensing performance of ZnO-CTAB. Among all six samples, the equimolar SnO_2-HMT exhibited greatest *m value* and R^2 *value* throughout increasing and decreasing RH. The reason that CTAB is less superior in hygroscopicity can be due to the hydrophobic environment caused by $-N(CH_3)_3^+$ headgroup of CTAB, leading to minimal water-surface interaction [53].

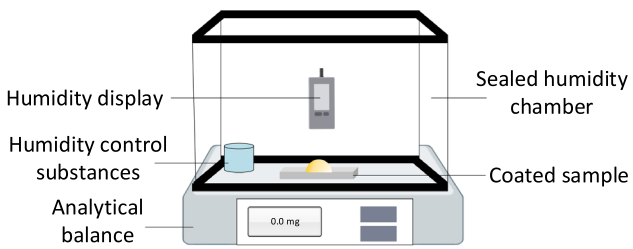

Fig. 8 Illustration of lab setup for hygroscopicity test

3.2 FTIR analysis

From the FTIR spectra as illustrated in Figs. 11 and 12, ranging from 4000 to 420 cm^{-1}, The O–H stretching vibration was represented by wavenumber 3000–3800 cm^{-1}, the Sn–O stretching vibration was represented by wavenumber 400–700 cm^{-1}, the Zn–O stretching vibration was represented by wavenumber 400–550 cm^{-1}, and the lattice vibrations of Zn − O bonds was represented by wavenumber 600–700 cm^{-1}. The individual peaks that represent presence of HMT functional group were ~ 820 cm^{-1}, ~ 1050 cm^{-1}, ~ 1250 cm^{-1}, and ~ 1670 cm^{-1} [54]. The individual peaks at ~ 2918 cm^{-1} and ~ 2850 cm^{-1} attributed to two different CH bands vibration of the $–CH_2$ group in CTAB [55]. The observed peaks at ~ 962 cm^{-1} and ~ 907 cm^{-1} corresponded to $C–N^+$ stretching modes of CTAB, while the peaks ranging from 1300 to 1680 cm^{-1} identified CH_2 scissoring mode of vibration of CTAB and O–H bending mode of water molecule [56].

The individual peaks that represent presence of HMT functional group can significantly be observed for sample with 0.010 and 0.020 M. On the contrary, the spectra were flat in this range of wavenumber for sample with 0.005 M, indicating minimal interaction between HMT and SnO_2. The CTAB sample with 0.020 M showed flat spectra of O–H stretching vibration due to poor water-surface interaction of the sample, which validated the result from the hygroscopicity test, where the *m value* was significantly lower compared to other samples.

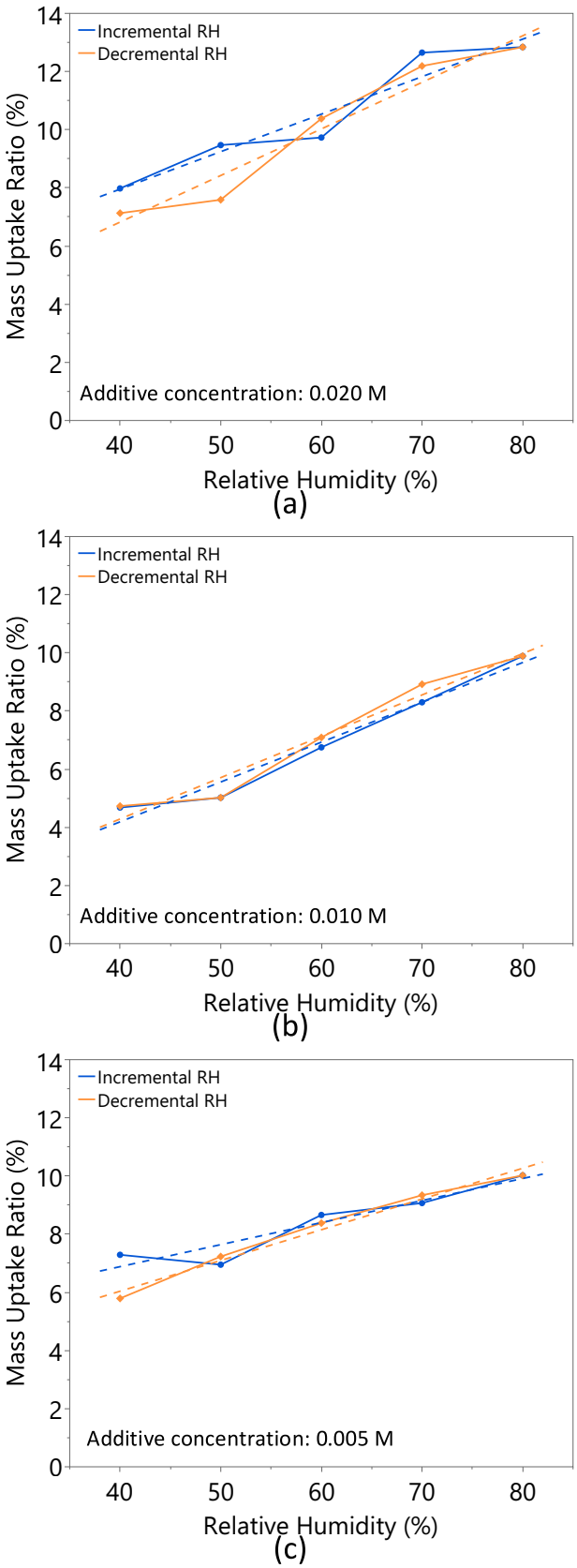

Fig. 9 Mass uptake ratio (%) of incremental and decremental humidity cycle from 40 – 80%RH for SnO_2-HMT with **a** 0.020 M, **b** 0.010 M, and **c** 0.005 M HMT concentrations

3.3 Microscope image

The selected magnification for microscope images was 20x, applied across all six samples to observe the change of surface structure with increasing and decreasing additive concentration as shown in Figs. 13 and 14. Increasing HMT concentration on SnO_2 led to aggregation and irregular surface structure. Whereas decreasing HMT concentration led to poor adhesion of the metal oxide, causing the material to crack and peel off from the substrate after annealing process. This can be due to incomplete surface modification or insufficient surface tension of SnO_2 with low additive concentration. A more uniform nanostructure can be obtained by maintaining the same concentration for both HMT and SnO_2, where potential nanoparticle formation was observed. With increasing CTAB concentration, a more compact nanoflake-like structure was observed, leading to the irregular surface of ZnO. Decreasing CTAB concentration causing formation of irregular nanoflake-like structure. With same CTAB and ZnO concentration, more uniform surface with formation of nanoflake-like structure can be clearly observed. These results demonstrate that the surface structure of metal oxide can be modified significantly under different additive concentrations.

3.4 FESEM analysis

All samples were subjected to FESEM analysis under ×2000 and ×30,000 magnification, as illustrated in Figs. 15 and 16, except SnO_2 sample with 0.005 M HMT concentration with poor adhesion of the metal oxide. The surface morphology was distinguished by the structural appearance of the nanostructure via FESEM images and was defined based on the similar morphology reported in previous work [23, 57]. Formation of nanoparticle can be clearly observed with samples of SnO_2 with equimolar HMT. The porosity of the nanoparticle can also be evidenced by FESEM analysis where a sponge-like nanostructure was formed. Whereas increasing additive concentration led to aggregation of SnO_2, where large, clustered particles were formed. The aggregation blocks diffusion pathways, decreasing

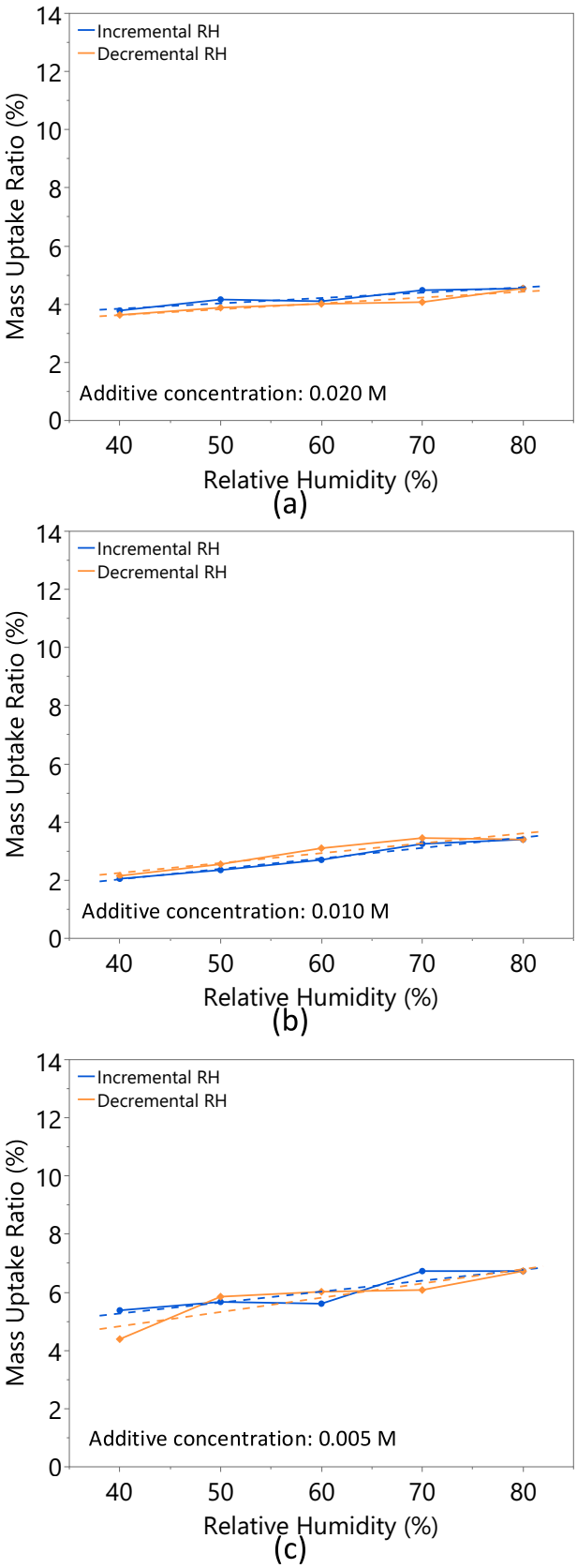

Fig. 10 Mass uptake ratio (%) of incremental and decremental humidity cycle from 40 to 80%RH for ZnO-CTAB with **a** 0.020 M, **b** 0.010 M, and **c** 0.005 M CTAB concentrations

the accessible porosity [58]. In addition, the clustered particles reduced effective surface area, limiting the accessibility of active sites [59]. The nanoflake across ZnO surface become compact with increased concentration of CTAB, whereas lower concentration of CTAB led to less organized nanoflake. The aggregation with increase additive concentration can be due to formation of excess micelles, caused by the hydrophilic head and hydrophobic tails of the additive [60]. Aggregated nanostructure often leads to reduce porosity and active sites, restricting the water-surface interaction [61]. The reduced water-surface interaction due to aggregation validated the hygroscopicity test result, where high additive concentration showed poor *m value* throughout the humidity cycle. On the contrary, with decrease additive concentration, minimal or no micelles formation as the additive concentration is below critical micelle concentration (CMC) [62], causing the formation of irregular nanoflake of ZnO. The FESEM cross-sectional view of equimolar SnO_2-HMT and ZnO-CTAB under ×300 magnification reported a nanostructure thickness of ~ 47 to 58 µm and ~ 87 to 97 µm. respectively, as shown in Fig. 17 and 18. The nanostructure exhibited high stability with no delamination detected upon exposure to humidity cycle.

3.5 TGA analysis

Few weight loss stages were observed from the TGA analysis result as illustrated in Figs. 19 and 20, where the initial stage around 100 °C was caused by dehydration of the samples and the second stage corresponded to the release of volatile organic additives [63]. The HMT decomposed at temperature around 237 °C [64], while the CTAB decomposed within the temperature range of 220 to 350 °C [65]. All SnO_2-HMT samples showed significant weight loss at the initial stage, indicating increase water desorption of the samples under high temperature conditions. With the increase of additive concentration, the weight loss percentage of second stage getting larger due to the decomposition of high HMT concentration. The ZnO-CTAB samples did not show significant dehydration at the initial

Table 3 Summary of hygroscopicity test result

Reactive materials	Additive concentration (M, molar)	*m* value incremental RH	*m* value decremental RH	R^2 value incremental RH	R^2 value decremental RH
SnO_2-HMT	0.020	0.1290	0.1602	0.92	0.95
	0.010	0.1370	0.1422	0.97	0.96
	0.005	0.0758	0.1057	0.89	0.98
ZnO-CTAB	0.020	0.0184	0.0201	0.89	0.91
	0.010	0.0360	0.0340	0.98	0.91
	0.005	0.0376	0.0491	0.83	0.81

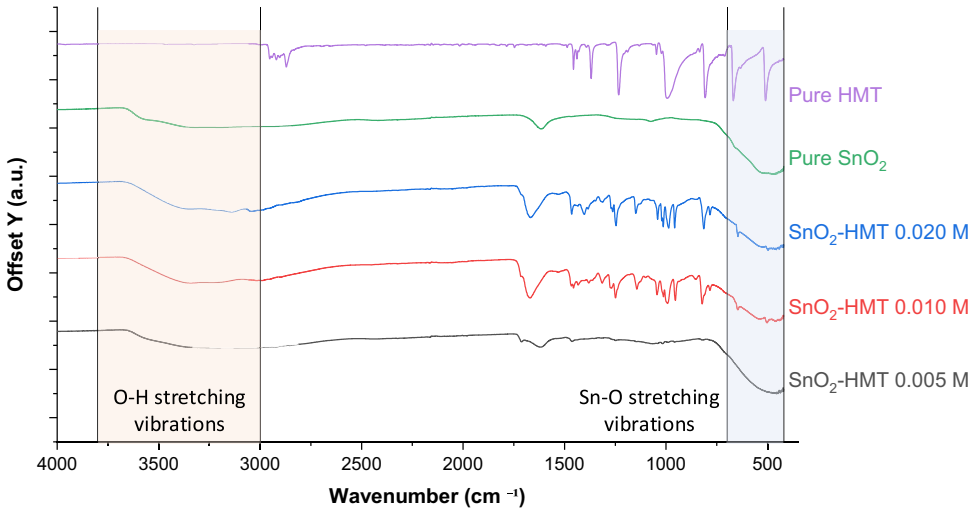

Fig. 11 FTIR analysis of 0.020 M, 0.010 M, and 0.005 M HMT concentrations with comparison with pure SnO_2 and HMT

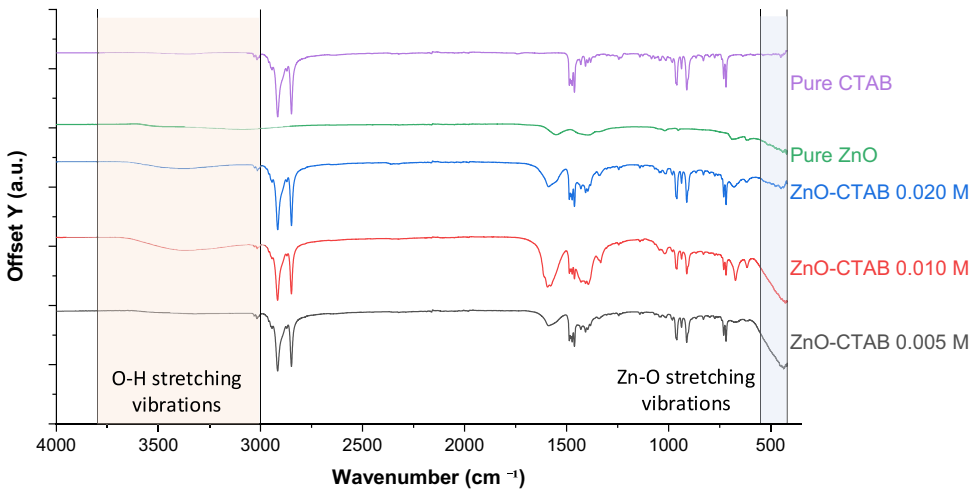

Fig. 12 FTIR analysis of 0.020 M, 0.010 M, and 0.005 M CTAB concentrations with comparison with pure ZnO and CTAB

stage, which validated the result of hygroscopicity test where lower m value of ZnO-CTAB was observed compared to SnO_2-HMT. However, the weight loss percentage at second stage is still significant with increase CTAB concentration.

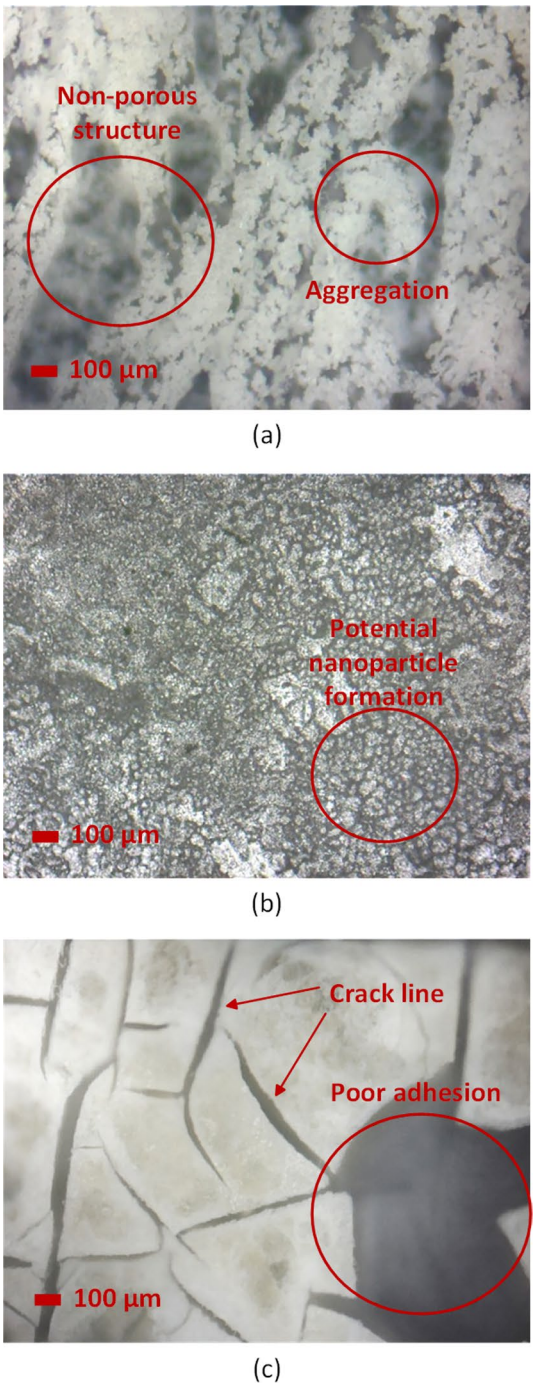

Fig. 13 Microscope image under ×20 magnification for **a** 0.020 M HMT, **b** 0.010 M HMT, and **c** 0.005 M HMT

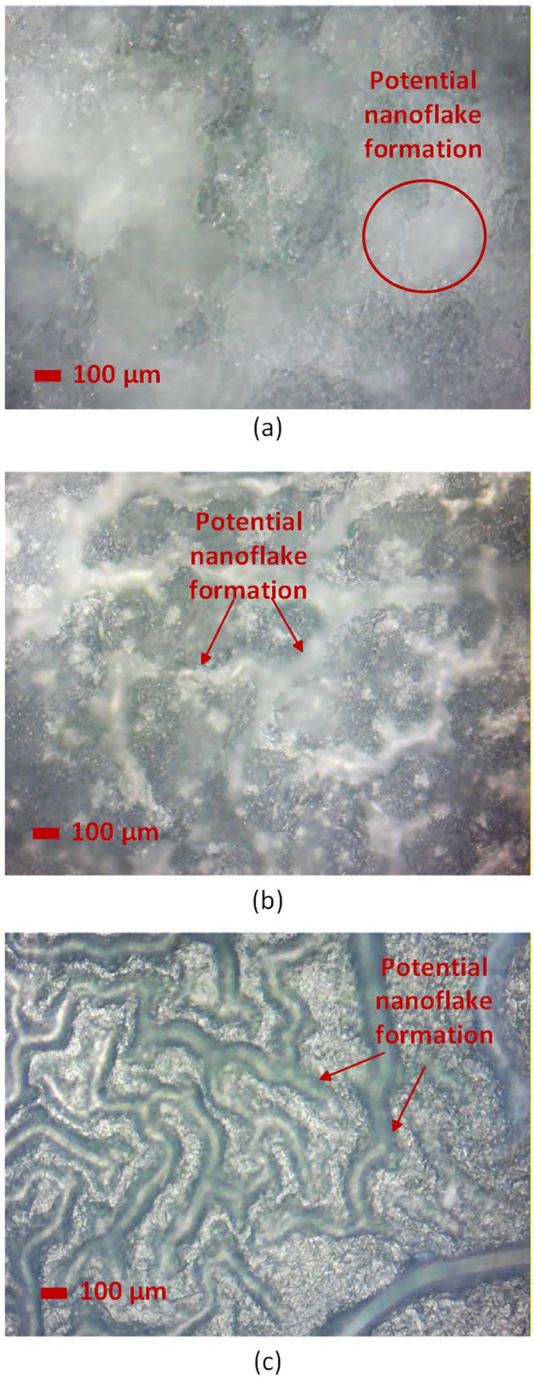

Fig. 14 Microscope image under ×20 magnification for **a** 0.020 M CTAB, **b** 0.010 M CTAB, and **c** 0.005 M CTAB

3.6 XRD

XRD analysis served as a validation test to analyze the crystallite size, which calculated based on the Scherrer equation, given by:

$$D = \frac{K\lambda}{\beta\cos\theta} \quad (2)$$

where D is the crystallite size, K is the Scherrer constant, λ is the X-ray wavelength (0.15406 nm), β is the

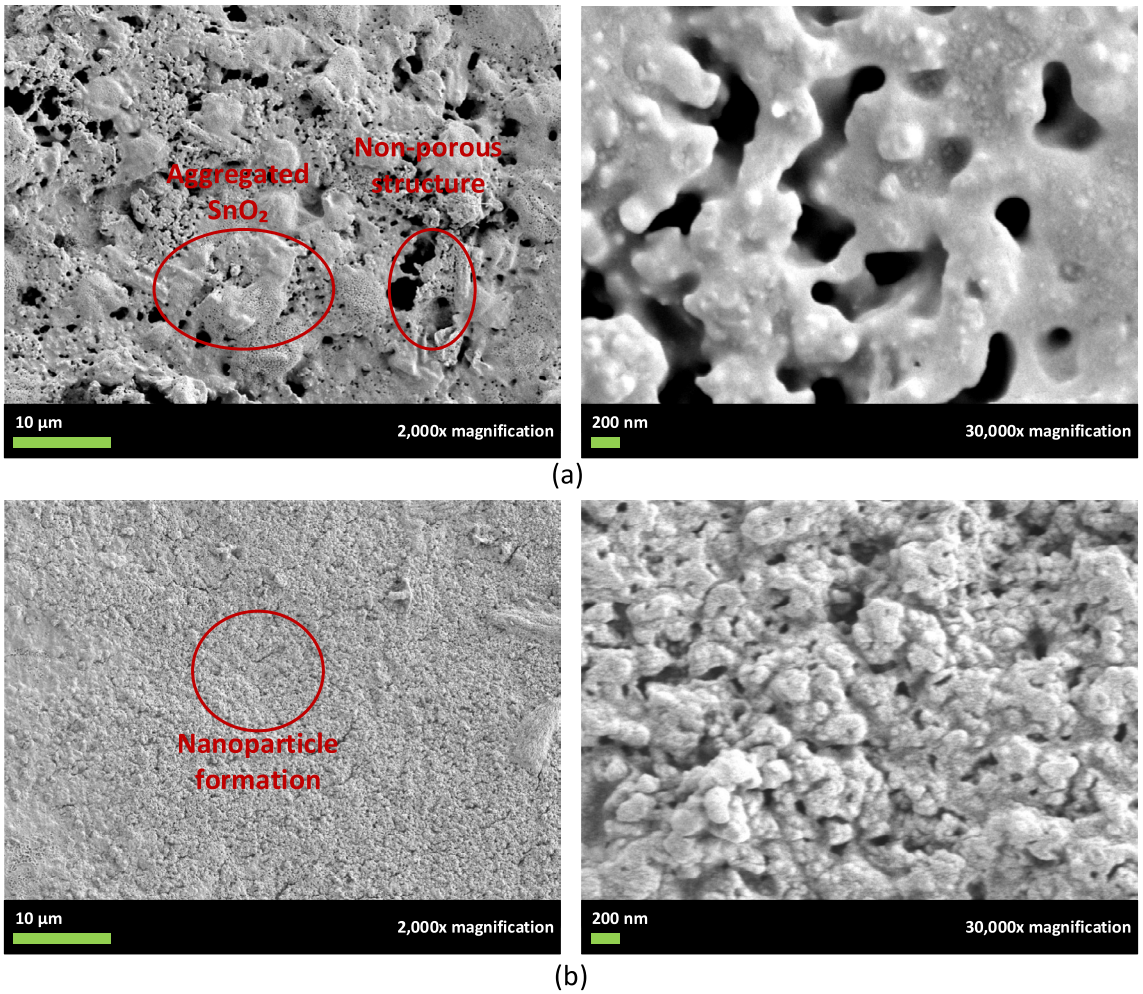

Fig. 15 FESEM images under ×2000 and ×30,000 magnification for **a** 0.020 M HMT, and **b** 0.010 M HMT

full width half maximum (FWHM) in radians, and θ is the Bragg angle in radians.

For the equimolar SnO_2–HMT, the major peak positions (2θ) at 23.197, 26.721, 32.900, 52.180, 58.496, and 73.367°, were corresponding to crystallite size of 57.938, 62.821, 55.232, 49.150, 37.943, and 90.066 nm. Similar result where crystallite size ~ 45 to 65 nm have been reported for SnO_2 nanostructures [66].

3.7 Optical spectrum analysis

The SnO_2-HMT coated FBG was exposed to humidity cycle from 40 to 80%RH and back to 40%RH, repeating same test conditions as per the hygroscopicity test. The shift in wavelength of every 10%RH was recorded as shown in Fig. 21. The wavelength shift was dominant by swelling of the reactive materials during water uptake, in which the swelling effect was transferred to the FBG and induced a strain change of the sensing region. This effect led to refractive index perturbation, which resulted in shift of wavelength captured by the optical spectrum analyzer (OSA). A sensitivity of 0.239 and 0.372 pm/%RH was obtained from three repetition cycles of incremental and decremental RH, respectively. The linear coefficient is > 0.97 throughout the humidity cycles. A previous study reported coating tilted FBG with PEDOT:PSS, a type of conductive polymer and reported sensitivity of 3.67 pm/%RH from 20 to 80%RH, with linear coefficient of 0.912 [67]. Another research demonstrated coating on a tilted FBG with polyvinyl alcohol (PVA) and graphene oxide (GO) and obtained sensitivity of − 0.24 pm/%RH from 35 to 85%RH [68]. The time elapsed for each 10% RH interval is shown in Fig. 22 with a 15 min waiting

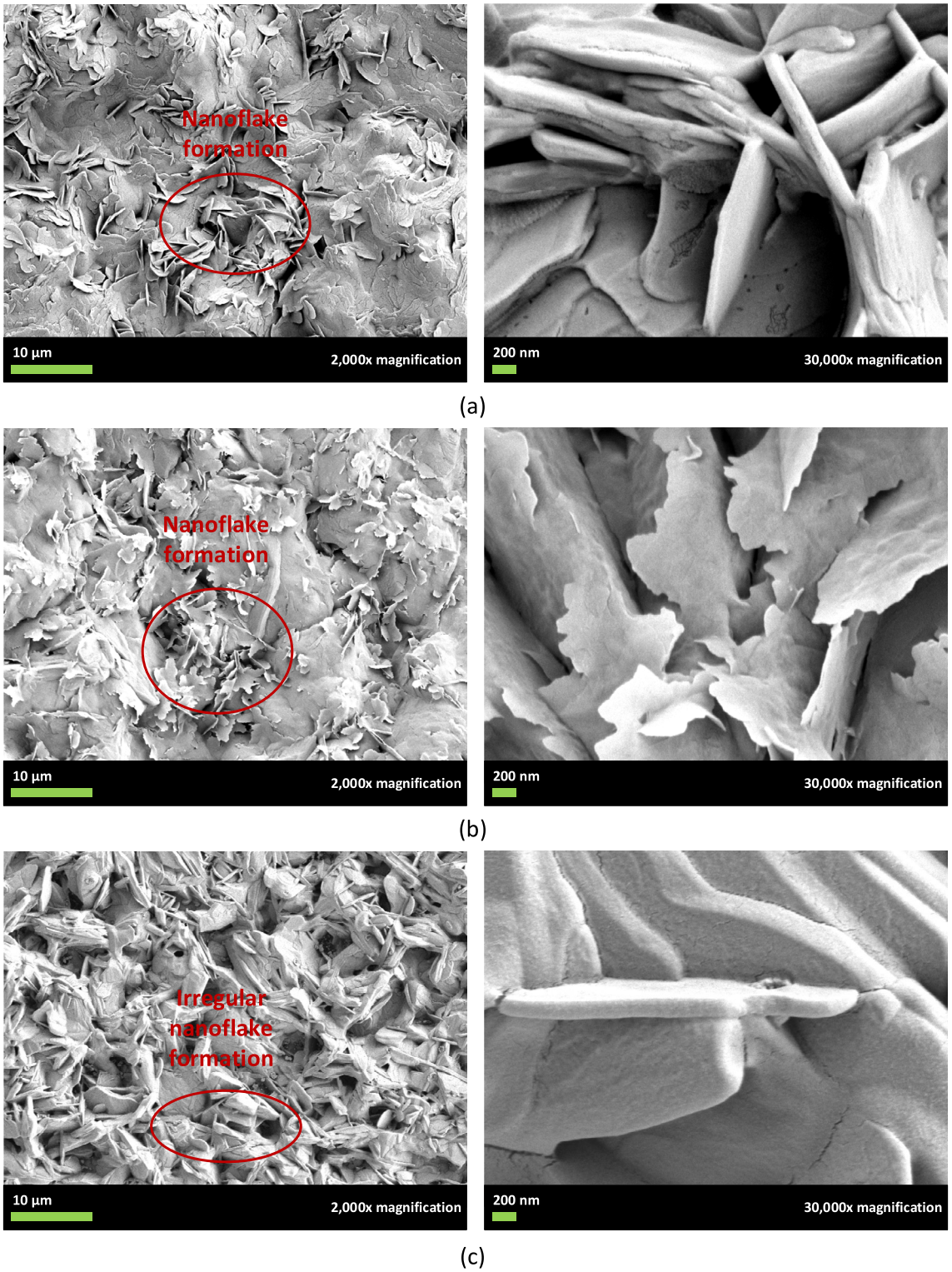

Fig. 16 FESEM images under ×2000 and ×30,000 magnification for **a** 0.020 M CTAB, **b** 0.010 M CTAB, and **c** 0.005 M CTAB

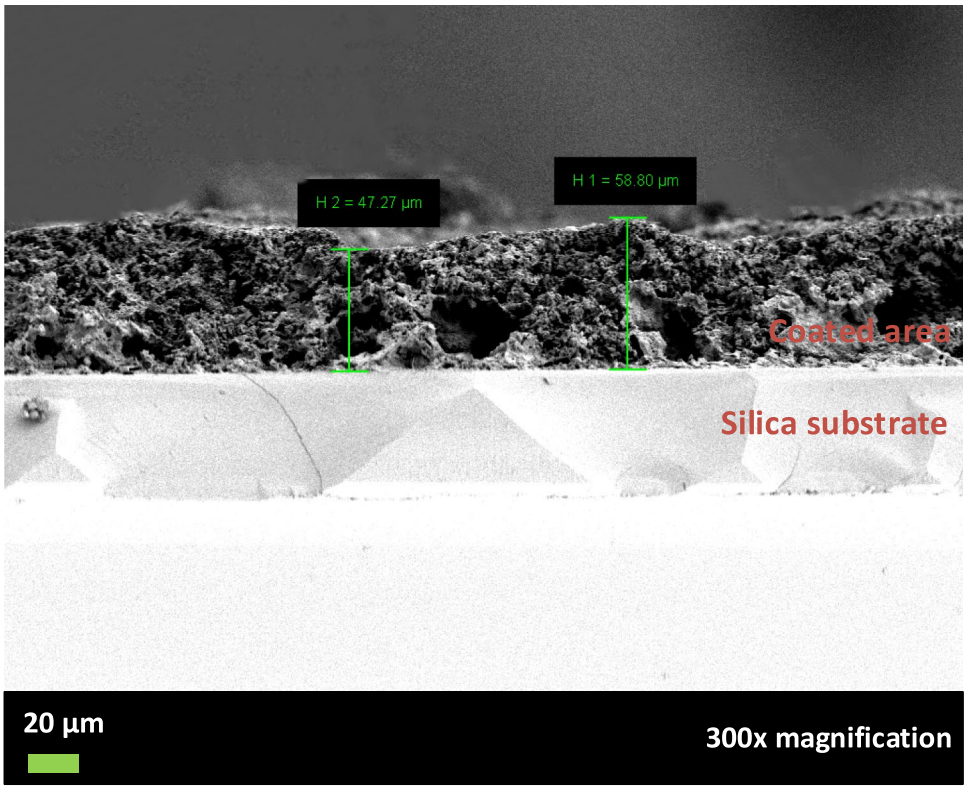

Fig. 17 FESEM cross-sectional view under ×300 magnification for 0.010 M HMT

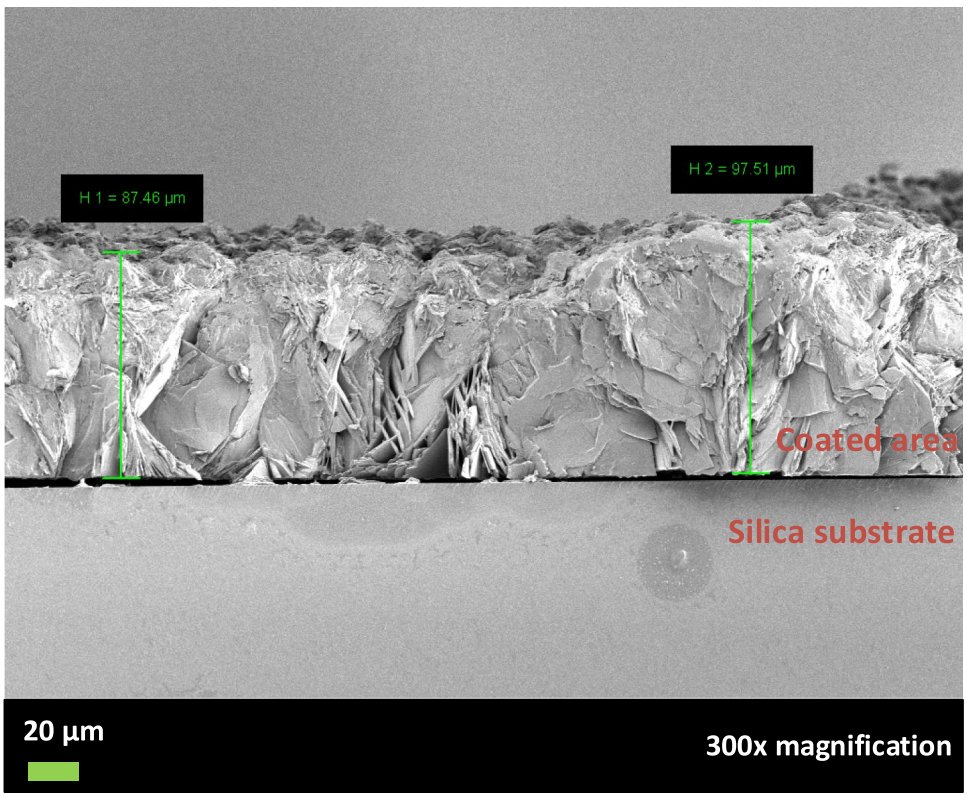

Fig. 18 FESEM cross-sectional view under ×300 magnification for 0.010 M CTAB

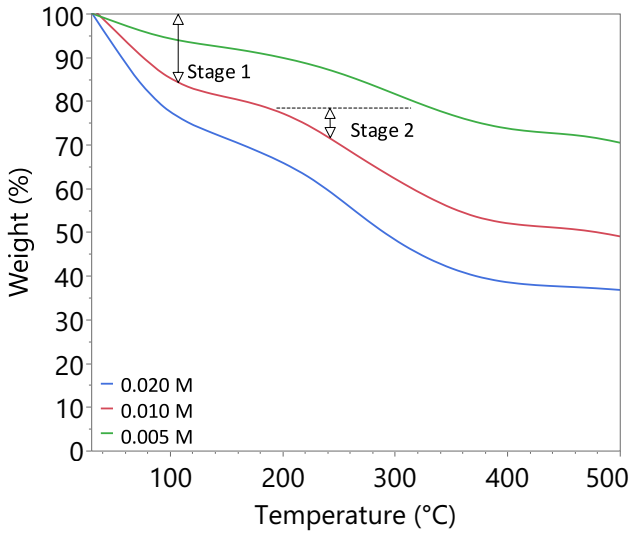

Fig. 19 TGA analysis of 0.020 M, 0.010 M, and 0.005 M HMT concentrations

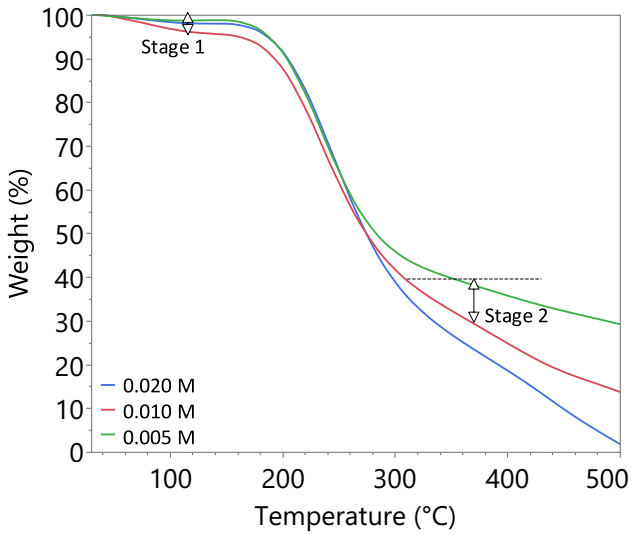

Fig. 20 TGA analysis of 0.020 M, 0.010 M, and 0.005 M CTAB concentrations

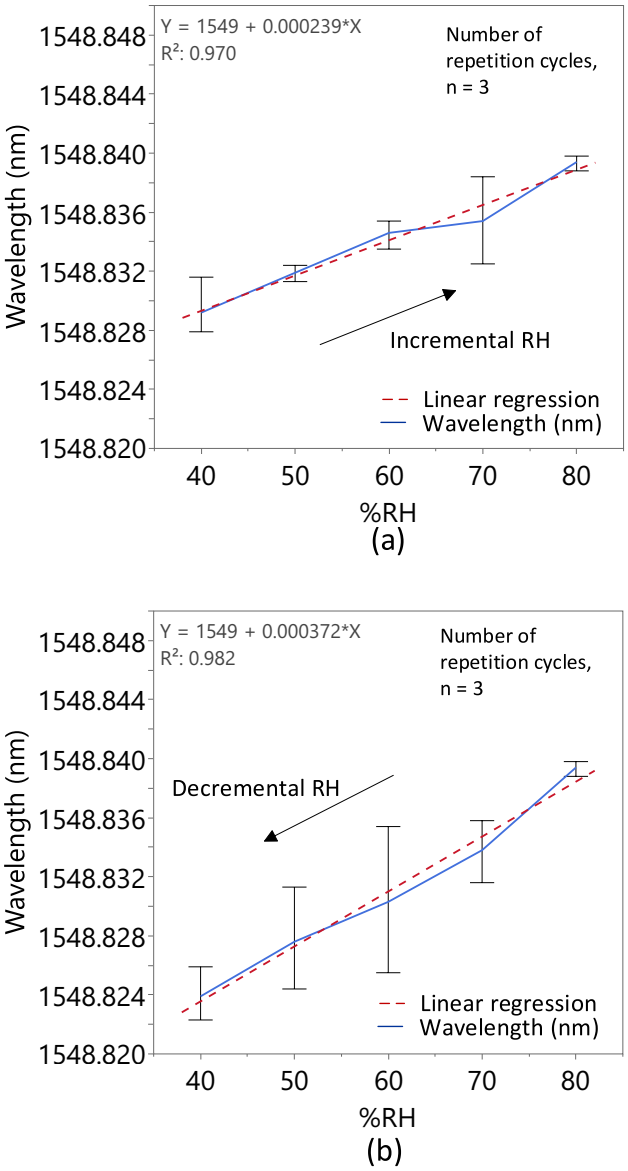

Fig. 21 Optical spectrum analysis of SnO_2-HMT coated TFBG with 0.010 M HMT concentration

time for wavelength shift. The calculated hysteresis, given by the ratio of difference between adsorption and desorption responses to the difference within the tested humidity range. The hysteresis at 70%RH close to 10.21%, increasing with decremental RH and reaching ~ 33.54% at 40%RH. The low hysteresis at high RH suggested limited improved reversibility of the sensor after exposure to humidity cycle. Whereas the increased hysteresis at low RH region can be due to the shrinkage of coating material did not transfer back to the sensing region with the same efficiency during desorption.

4 Conclusion

The paper summarized the impact of HMT and CTAB concentration towards the hygroscopicity, structural, morphology, and thermal properties of SnO_2 and ZnO. Both SnO_2-HMT and ZnO-CTAB showed improved hygroscopicity under equimolar additive concentration. A more uniform surface

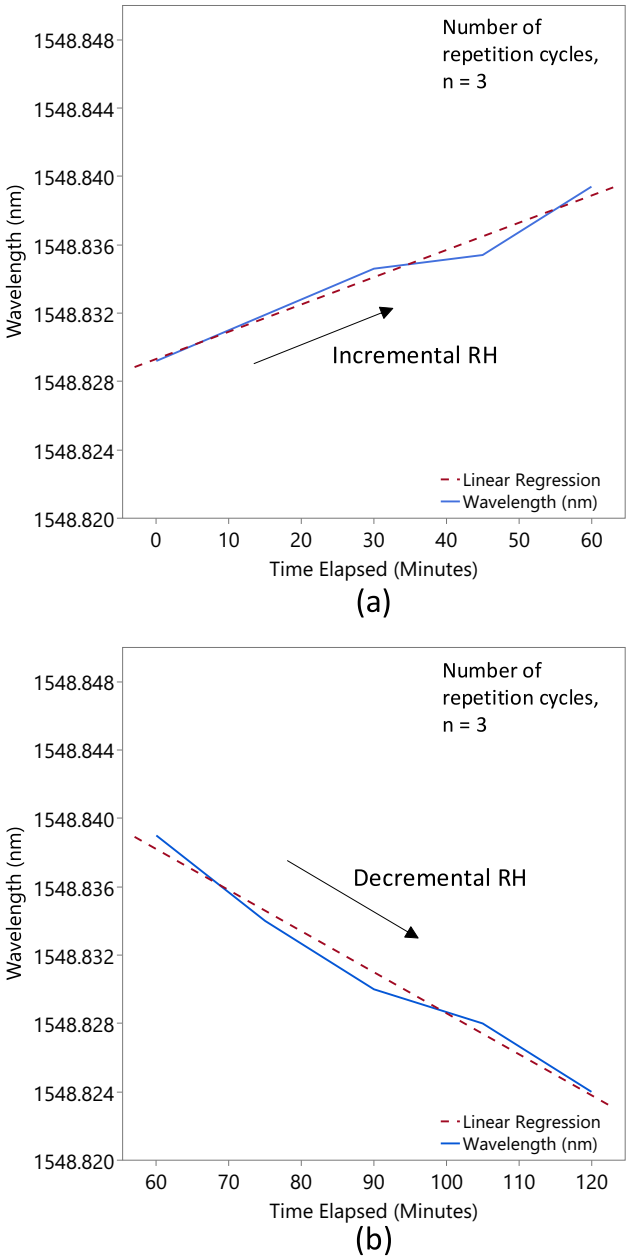

Fig. 22 Time elapsed of SnO_2-HMT coated TFBG with 0.010 M HMT concentration

morphology was formed under concentration of 0.010 M for both additive and reactive material. Maintaining the equimolar concentrations between additive and reactive material promotes stoichiometric balance, establishing a dynamic equilibrium that allows optimal interaction for controlled nucleation and uniform growth of nanostructure [69]. Whereas increasing the additive concentration led to excess formation of micelles and vice versa, causing the irregular surface morphology which jeopardized the water adsorption and desorption mechanism. The thermal properties of reactive materials were also impacted by additive concentration, where higher concentration increases the decomposition rate, reducing the thermal stability of the materials. By optimizing the additive concentration, enhanced humidity sensing can be achieved, with a sensitivity up to 0.372 pm/RH and fitting coefficient > 0.97. Further research can be carried out by coating the additive-enhanced reactive materials via different coating methods onto sensing devices for fast response and recovery time, good repeatability and stability, and increase sensitivity, enabling real-time detection in humidity sensitive industry including agriculture, food and beverage, and semiconductor [70, 71].

Author contributions

Conceptualization, S.P.K.; Methodology, S.P.K.; Validation, S.P.K.; Formal analysis, S.P.K.; Investigation, S.P.K.; Resources, S.B.A.A. and K.Y.C.; Data curation, S.P.K.; Writing—original draft, S.P.K.; Writing—review & editing, Y.I.G.; Visualization, S.P.K.; Supervision, Y.I.G.; Project administration, Y.I.G.; Funding acquisition, Y.I.G. and M.L.D.W. All authors have read and agreed to the published version of the manuscript.

Funding

This work was supported by the Ministry of Higher Education Malaysia through the Fundamental Research Grant Scheme (FRGS) under Grant FRGS/1/2023/TK08/HWUM/02/2.

Data availability

Data is contained within the article.

Declarations

Conflicts of interest The authors declare no conflict of interest.

Appendix

See Table 4 and Figs. 23 and 24.

Table 4 Summary of mass change in reactive material under different additive concentration

Reactive materials	Additive concentration (M, molar)	Relative humidity (%RH)	Mass (mg), incremental RH	Mass (mg), decremental RH
SnO_2-HMT	0.020	40	55.50	55.07
		50	56.27	55.30
		60	56.40	56.73
		70	57.90	57.67
		80	58.00	58.00
	0.010	40	72.33	72.37
		50	72.57	72.57
		60	73.77	74.00
		70	74.83	75.27
		80	75.93	75.93
	0.005	40	52.47	51.73
		50	52.30	52.43
		60	53.13	53.00
		70	53.33	53.47
		80	53.80	53.80
ZnO-CTAB	0.020	40	109.70	109.53
		50	110.10	109.80
		60	110.03	109.93
		70	110.43	110.00
		80	110.50	110.50
	0.010	40	68.07	68.13
		50	68.27	68.40
		60	68.50	68.77
		70	68.87	69.00
		80	68.97	68.97
	0.005	40	60.07	59.50
		50	60.23	60.33
		60	60.20	60.43
		70	60.83	60.47
		80	60.83	60.83

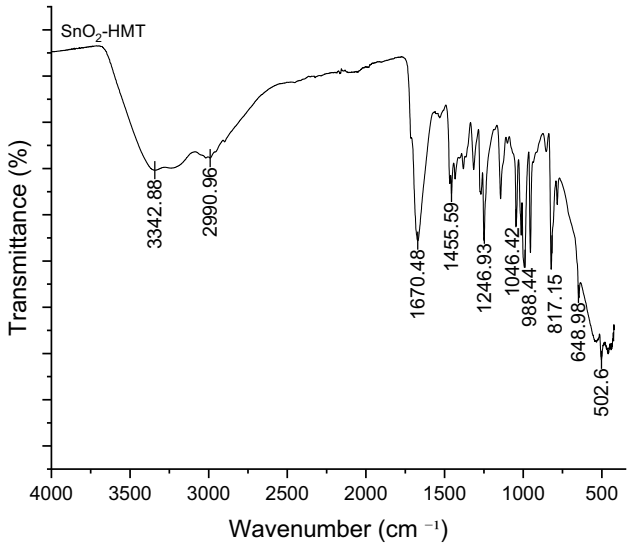

Fig. 23 FTIR analysis of 0.010 M HMT concentrations

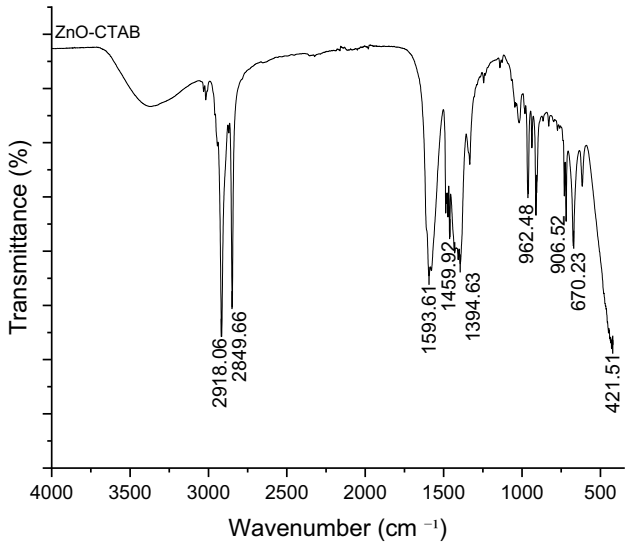

Fig. 24 FTIR analysis of 0.010 M CTAB concentrations

References

1. J. Qian, R. Tan, M. Feng, W. Shen, D. Lv, W. Song, Humidity sensing using polymers: a critical review of current technologies and emerging trends. Chemosensors **12**, 230 (2024)
2. J.-M. Tulliani, B. Inserra, D. Ziegler, Carbon-based materials for humidity sensing: a short review. Micromachines **10**, 232 (2019)
3. T. Xie, A.F. Abdul Rahman, A. Abu Bakar, A. Arsad, Design and optimization of metal oxide-based humidity sensors: a review on mechanisms and material engineering. J. Cluster Sci. **36**, 148 (2025)
4. S. Kano, H. Mekaru, Nonporous inorganic nanoparticle-based humidity sensor: evaluation of humidity hysteresis and response time. Sensors **20**, 3858 (2020)
5. S.P. Kok, Y.I. Go, M.L.D. Wong, Effect of hygroscopic and electronic materials, challenges, and sensing requirements in humidity-controlled industry. J. Electron. Mater. **54**, 6960 (2025). https://doi.org/10.1007/s11664-025-12140-x
6. B. Kuswandi, M. Moradi, Sensor trends in beverages packaging, in *Trends in beverage packaging*. (Academic Press, 2019), pp.279–302
7. J.E. Hyun, J.H. Kim, Y.S. Choi, E.M. Kim, J.C. Kim, S.Y. Lee, Evaluation of microbial quality of dried foods stored at different relative humidity and temperature, and effect of packaging methods. J. Food Saf. **38**, 12433 (2018)
8. R. Lufu, A. Ambaw, U.L. Opara, The influence of internal packaging (liners) on moisture dynamics and physical and physiological quality of pomegranate fruit during cold storage. Foods **10**, 1388 (2021)
9. X. Zuo, S. Cao, W. Jia, Z. Zhao, P. Jin, Y. Zheng, Near-saturated relative humidity alleviates chilling injury in zucchini fruit through its regulation of antioxidant response and energy metabolism. Food Chem. **351**, 129336 (2021)

10. C. Maraveas, T. Bartzanas, Application of Internet of Things (IoT) for optimized greenhouse environments. AgriEngineering **3**, 954 (2021)
11. B. Rabbi, Z.-H. Chen, S. Sethuvenkatraman, Protected cropping in warm climates: a review of humidity control and cooling methods. Energies **12**, 2737 (2019)
12. S. Zhao, Z. Wu, M. Lai, M. Zhao, B. Lin, Determination of optimum humidity for air-curing of cigar tobacco leaves during the browning period. Ind. Crops Prod. **183**, 114939 (2022)
13. D. Limwiwattana, K. Tongkhao, K. Na Jom, Effect of sprouting temperature and air relative humidity on metabolic profiles of sprouting black gram (*Vigna mungo* L.). J. Food Process. Preserv. **40**, 306 (2016)
14. A. Saleem, S. Anwar, T. Nawaz et al., Securing a sustainable future: the climate change threat to agriculture, food security, and sustainable development goals. J. Umm Al-Qura University Appl. Sci. **11**, 595 (2025)
15. S. Guo, I. Radecka, A.M. Eissa, E. Ivanov, Z. Stoeva, F. Tchuenbou-Magaia, Recent advances in carbon-based sensors for food and medical packaging under transit: a focus on humidity, temperature, mechanical, and multifunctional sensing technologies—a systematic review. Materials **18**, 1862 (2025)
16. M. Weston, S. Geng, R. Chandrawati, Food sensors: challenges and opportunities. Adv. Mater. Technol. **6**, 2001242 (2021)
17. M.I. Abdulraheem, Y. Xiong, W. Zhang, H. Chen, H. Zhang, J. Hu, Recent applications of fiber Bragg grating sensors in humidity and water content detection in agriculture: a comprehensive review of development, challenges, and future trends. Int. J. Precis. Eng. Manuf. **25**, 1499 (2024)
18. M. Kumari, N. Dhariwal, P. Yadav, V. Kumar, O. Thakur, Urea modified Cu-doped LaFeO3 nano-particles for humidity sensing with contactless moisture detection for medical and agricultural application. Sens. Actuators B Chem. **423**, 136749 (2025)
19. S. Patil, N. Ramgir, S. Mukherji, V.R. Rao, PVA modified ZnO nanowire based microsensors platform for relative humidity and soil moisture measurement. Sens. Actuators B Chem. **253**, 1071 (2017)
20. S. Khasim, A. Pasha, N. Badi, M. Lakshmi, S. Al-Ghamdi, H.A. AL-Aoh, PVA treated PEDOT-PSS: TiO2 nanocomposite based high-performance sensors towards detection of relative humidity and soil moisture content for agricultural applications. J. Polym. Environ. **29**, 612 (2021)
21. M.A. Riza, Y.I. Go, R.R. Maier, S.W. Harun, S.B. Anas, Hygroscopic materials and characterization techniques for fiber sensing applications: a review. Sens. Mater. **32**, 3755 (2020)
22. Y.-F. Zhao, Y.-P. Sun, X. Yin et al., Effect of surfactants on the microstructures of hierarchical SnO2 blooming nanoflowers and their gas-sensing properties. Nanoscale Res. Lett. **13**, 250 (2018)
23. C.-D. Villa-Miranda, F.J. Carranza-Chávez, D. Sauceda-Carvajal, A.-K. Cuentas-Gallegos, I. Zavala-Guillén, H.A. Borbón-Núñez, Employment of low-temperature concentrated solar heat to synthesize Zinc Oxide nanostructures. J. Nanotechnol. **2024**, 4916705 (2024)
24. A. Mahmud, A.A. Khan, P. Voss, T. Das, E. Abdel-Rahman, D. Ban, A high performance and consolidated piezoelectric energy harvester based on 1D/2D hybrid Zinc Oxide nanostructures. Adv. Mater. Interfaces **5**, 1801167 (2018)
25. H. Jeong, Y. Noh, D. Lee, Highly stable and sensitive resistive flexible humidity sensors by means of roll-to-roll printed electrodes and flower-like TiO2 nanostructures. Ceram. Int. **45**, 985 (2019)
26. W. Akram, S. Iqbal, Z. Abbas et al., Metal organic framework based humidity sensing: stability, performance, and IoT integration. J. Sci. Adv. Mater. Devices (2025). https://doi.org/10.1016/j.jsamd.2025.100972
27. S.P. Kok, Y.I. Go, W. Xu, M.D. Wong, A review of nanostructure coating techniques to achieve high-precision optical fiber sensing applications. Nanomanufacturing **4**, 214 (2024). https://doi.org/10.3390/nanomanufacturing4040015
28. S. Yu, H. Zhang, C. Lin, M. Bian, The enhancement of humidity sensing performance based on Eu-doped ZnO. Curr. Appl. Phys. **19**, 82 (2019)
29. H.A. Saputra, Electrochemical sensors: basic principles, engineering, and state of the art. Monatsh. Chem. **154**, 1083 (2023)
30. A.F. Staerz, H.G. Seo, H.L. Tuller, Surface electron modulation of metal oxide-based electrochemical devices by surface additives—linking sensors and fuel cells. J. Am. Ceram. Soc. **107**, 1959 (2024)
31. M.S. Bakshi, How surfactants control crystal growth of nanomaterials. Cryst. Growth Des. **16**, 1104 (2016)
32. R. Sarkar, A. Pal, A. Rakshit, B. Saha, Properties and applications of amphoteric surfactant: a concise review. J. Surfactants Deterg. **24**, 709 (2021)
33. Z. Wang, G. Shi, F. Zhang et al., Amphoteric surfactant promoted three-dimensional assembly of graphene micro/nanoclusters to accomodate Pt nanoparticles for methanol oxidation. Electrochim. Acta **160**, 288 (2015)
34. L.Y. Zakharova, T.N. Pashirova, S. Doktorovova et al., Cationic surfactants: self-assembly, structure-activity

correlation and their biological applications. Int. J. Mol. Sci. **20**, 5534 (2019)
35. Z. Singh, I. Singh, CTAB surfactant assisted and high pH nano-formulations of CuO nanoparticles pose greater cytotoxic and genotoxic effects. Sci. Rep. **9**, 5880 (2019)
36. H. Avireddy, H. Kannan, P. Shankar, G.K. Mani, A.J. Kulandaisamy, J.B.B. Rayappan, Non-mutually exclusive dual role of hexamethylenetetramine on the growth of ZnO nanostructures and their sensing footprints. Mater. Chem. Phys. **212**, 394 (2018)
37. S.K. Mishra, U. Tripathi, R. Awasthi et al., CTAB mediated synthesis of ZnO nanoparticles: structural, optical and enhanced blue-green optical emission. Mater. Today Proc. **46**, 2229 (2021)
38. T. Sreethawong, S. Ngamsinlapasathian, S. Yoshikawa, Surfactant-aided sol–gel synthesis of mesoporous-assembled TiO2–NiO mixed oxide nanocrystals and their photocatalytic azo dye degradation activity. Chem. Eng. J. **192**, 292 (2012)
39. J. Jasmin, P. Anilkumar, S. Deepak, Synthesis, analysis and characterization of surfactant-assisted TiO2 nanoparticles for ammonia gas sensor applications. Ceram. Int. **50**, 52262 (2024)
40. A. Kumar, P. Kumari, M.S. Kumar, G. Gupta, D. Shivagan, K. Bapna, SnO2 nanostructured thin film as humidity sensor and its application in breath monitoring. Ceram. Int. **49**, 24911 (2023)
41. F. Li, P. Li, H. Zhang, Preparation and research of a high-performance ZnO/SnO2 humidity sensor. Sensors **22**, 293 (2021)
42. P. Malik, S. Duhan, R. Malik, A high-performance humidity sensor based on 3D porous SnO 2-encapsulated MCM-48 for real-time breath monitoring and contactless gesture detection. Mater. Adv. **5**, 2510 (2024)
43. D.A. Peixoto, S.C. Silva, P.H. Borges, R.C. Lima, E. Nossol, Hydrothermal synthesis as a versatile tool for the preparation of metal hexacyanoferrates: a review. J. Mater. Sci. **58**, 2993 (2023)
44. S.P. Kok, Y.I. Go, S.B. Ahmad Anas, M.D. Wong, K.Y. Chan, Synthesis of new metal oxide sensing materials via the HMT technique for humidity control in the pharmaceutical industry. Discov. Sens. **2**, 1 (2026). https://doi.org/10.1007/s44397-025-00033-x
45. C.V. Lacombre, G. Bouvet, D. Trinh, S. Mallarino, S. Touzain, Effect of pigment and temperature onto swelling and water uptake during organic coating ageing. Prog. Org. Coat. **124**, 249 (2018)
46. S.V. Glass, C.R. Boardman, E.E. Thybring, S.L. Zelinka, Quantifying and reducing errors in equilibrium moisture content measurements with dynamic vapor sorption (DVS) experiments. Wood Sci. Technol. **52**, 909 (2018)
47. S.C. Medina, A.S. Farinha, A.-H. Emwas, A. Tabatabai, T. Leiknes, A fundamental study of adsorption kinetics of surfactants onto metal oxides using quartz crystal microbalance with dissipation (QCM-D). Colloids Surf. A Physicochem. Eng. Aspects **586**, 124237 (2020)
48. H. Zhao, X. Li, S. Lei et al., Quartz crystal microbalance (QCM)-based portable system for visualizing reaction kinetics in secondary chemistry education. J. Chem. Educ. **102**, 3661 (2025)
49. American Society for Testing and Materials (2020)
50. Y. Tkachenko, P. Niedzielski, FTIR as a method for qualitative assessment of solid samples in geochemical research: a review. Molecules **27**, 8846 (2022)
51. Y. Liu, Y. Li, P. Xu, C. Yu, Temperature and lateral pressure sensing using a sagnac sensor based on cascaded tilted grating and polarization-maintaining fibers. Sensors **24**, 6779 (2024)
52. K. Yanagita, J. Hwang, J.A. Shamim et al., Kinetics of water vapor adsorption and desorption in MIL-101 metal–organic frameworks. J. Phys. Chem. C **123**, 387 (2018)
53. J.A. Long, B.M. Rankin, D. Ben-Amotz, Micelle structure and hydrophobic hydration. J. Am. Chem. Soc. **137**, 10809 (2015)
54. S.P. Kok, Y.I. Go, S.B.A. Anas, M.D. Wong, K.Y. Chan, Additive-enhanced SnO2 FBG sensor with optimized annealing time, temperature, and multilayer coating for high-performance humidity sensing. Nanomaterials **15**, 1508 (2025). https://doi.org/10.3390/nano15191508
55. S.A. Elfeky, S.E. Mahmoud, A.F. Youssef, Applications of CTAB modified magnetic nanoparticles for removal of chromium (VI) from contaminated water. J. Adv. Res. **8**, 435 (2017)
56. B. Nikoobakht, M.A. El-Sayed, Evidence for bilayer assembly of cationic surfactants on the surface of gold nanorods. Langmuir **17**, 6368 (2001)
57. C. Zhao, J. Zhang, Y. Hu et al., In-situ microfluidic controlled, low temperature hydrothermal growth of nanoflakes for dye-sensitized solar cells. Sci. Rep. **5**, 17750 (2015)
58. N. Delouche, J. Van Doorn, T. Kodger, A. Schofield, J. Sprakel, H. Tabuteau, The contribution of colloidal aggregates to the clogging dynamics at the pore scale. J. Membr. Sci. **635**, 119509 (2021)
59. Z. Lu, B. Chen, C.Y. Leung, Z. Li, G. Sun, Aggregation size effect of graphene oxide on its reinforcing efficiency to cement-based materials. Cem. Concr. Compos. **100**, 85 (2019)

60. M. Stack, D. Parikh, H. Wang et al., in *Electrospinning: nanofabrication and applications*. ed. by B. Ding, X. Wang, J. Yu (William Andrew Publishing, 2019)
61. L. Shang, H. Yu, X. Huang et al., Well-dispersed ZIF-derived Co, N-co-doped carbon nanoframes through mesoporous-silica-protected calcination as efficient oxygen reduction electrocatalysts. Adv. Mater. **28**, 1668 (2016)
62. M.K. Hasan, T. Khandaker, M.S. Hossain, A.B. Ibrahim, S. Kawaguchi, Determination of critical micelle concentration of amphiphilic surfactants: a comprehensive review. Anal. Chem. (2026). https://doi.org/10.1021/acs.analchem.5c06191
63. J. Chen, Y. Wang, X. Lang, X. Ren, S. Fan, Comparative evaluation of thermal oxidative decomposition for oil-plant residues via thermogravimetric analysis: thermal conversion characteristics, kinetics, and thermodynamics. Bioresour. Technol. **243**, 37 (2017)
64. G. Rao, W. Feng, J. Zhang et al., Simulation approach to decomposition kinetics and thermal hazards of hexamethylenetetramine. J. Therm. Anal. Calorim. **135**, 2447 (2019)
65. S.-H. Wu, D.-H. Chen, Synthesis of high-concentration Cu nanoparticles in aqueous CTAB solutions. J. Colloid Interface Sci. **273**, 165 (2004)
66. P. Khaenamkaew, D. Manop, C. Tanghengjaroen, W. Palakawong Na Ayuthaya, Crystal structure, lattice strain, morphology, and electrical properties of SnO2 nanoparticles induced by low calcination temperature. Adv. Mater. Sci. Eng. **2020**, 3852421 (2020)
67. H.-Y. Wen, W.-Y. Huang, T.-S. Huang, Y.-C. Hsu, C.-C. Chiang, Comparison of the sensing mechanisms and capabilities of three functional materials surface-modified TFBG sensors. AIP Adv. **10**, 065319 (2020)
68. L. Deng, H. Sun, J. Xi et al., Simulation and experiment of tilted fiber bragg grating humidity sensor coated with PVA/GO nanofiber films by electrospinning. Sensors **25**, 7386 (2025)
69. P.L. Chaudhari, D.R. Patil, S.A. More et al., Study the opto-structural properties of the mixed halide perovskite films by maintaining an equimolar stoichiometry of organic halide and metal halide composition in the precursor solution. J. Mater. Sci. Mater. Electron. **37**, 199 (2026)
70. B. Du, X. Mu, S. Liu et al., A new strategy for real-time humidity detection: polymer-coated optical waveguide sensor. Chemosensors **10**, 63 (2022)
71. Z. Ahmad, M. Abbas, I. Gunawan, R. Shakoor, F. Ubaid, F. Touati, Electro-sprayed PVA coating with texture-enriched surface morphology for augmented humidity sensing. Prog. Org. Coat. **117**, 7 (2018)